

Heavy-ion beam illumination on a direct-driven pellet in heavy-ion inertial fusion

Tetsuo Someya,^{1,*} Aleksandar I. Ogoyski,^{1,2} Shigeo Kawata,^{1,†} and Toru Sasaki¹

¹*Department of Energy and Environmental Science, Utsunomiya University, Utsunomiya 321-8585, Japan*

²*Department of Physics, Varna Technical University, Varna 9010, Bulgaria*

(Received 29 July 2003; published 8 April 2004)

Key issues in heavy-ion beam (HIB) inertial confinement fusion (ICF) include an accelerator design for an intense HIB, an efficient HIB transport, a HIB-target interaction, a reactor design, and so on. In this paper, three-dimensional computer simulations are performed for a HIB irradiation onto a direct-driven spherical fuel pellet in HIB-ICF in order to clarify dependence of multi-HIB illumination nonuniformity on parameter values of HIB illumination. For various beam parameters and reactor chamber radii we investigate the energy deposition nonuniformity using 12, 20, 32, 60, 92, and 120-beam irradiation systems. In this study, the effects of HIB temperature, HIB illumination systems, HIB emittance, and pellet temperature on the HIB illumination nonuniformity are also evaluated. In addition, the nonuniformity growth due to a little pellet displacement from a reactor chamber center is investigated. The calculation results demonstrate that we can realize a rather low nonuniform energy deposition, for example, less than 2.0 % even for a 32-beam irradiation system.

DOI: 10.1103/PhysRevSTAB.7.044701

PACS numbers: 52.58.Hm, 34.50.Bw, 28.52.Cx

I. INTRODUCTION

Key issues in heavy-ion beam (HIB) inertial confinement fusion (ICF) include an accelerator design for intense HIBs, efficient HIB transport, a HIB-target interaction, a reactor design, and so on [1–11]. In this study, we focus on a HIB-target interaction in ICF. In HIB-ICF, the beam irradiation nonuniformity on a direct-driven fuel pellet must be suppressed under a few percent in order to achieve a symmetric fuel pellet implosion [7,12–17]. Therefore a multi-HIB illumination is required to achieve a low beam nonuniformity in the pellet implosion. On the other hand, the total HIB number should be restricted to a realistic number, for example, less than a few hundred beams. Therefore, in this study, we simulate a HIB illumination on the spherical direct-driven target using 12, 20, 32, 60, 92, and 120-beam irradiation systems. In Sec. II we present details of beam illumination.

In heavy-ion fusion (HIF), the HIB space charge should be neutralized by a plasma [10] or an insulator guide [9] or other methods [11] at the final transport region in order to suppress the beam divergence and the emittance growth; the HIB neutralization methods have been proposed and studied. After the HIB final transport, the neutralized HIBs illuminate a fuel target. In the fuel pellet implosion the HIB energy deposition nonuniformity should be suppressed to less than a few percent [7,15–17] in order to realize a stable implosion and to obtain a high ρR of the compressed fuel core. The requirement for the implosion uniformity has also been well studied, and analyses of instabilities, including the Rayleigh-Taylor instability, have been performed intensively in the

indirect-driven and the direct-driven implosion schemes. Each implosion scheme has merits and demerits [3–5,7,15,18]: the indirect-driven scheme may be robust against the beam nonuniformity, though its structure may be complicated and may be relatively expensive. The direct-driven pellet structure may be simple, though the scheme may be sensitive to the HIB illumination nonuniformity.

In HIF research a study of a realistic HIBs illumination nonuniformity remains between the final HIB transport and the fuel pellet implosion studies and is at present essentially important for progress in HIF studies. Therefore in this paper we perform three-dimensional analyses of the HIB illumination nonuniformity in HIB-ICF in order to know the detailed information of energy nonuniformity on a spherical fuel target.

The HIB illuminates the spherical target and deposits its energy on the target. We calculate the deposition energy on the spherical target according to a stopping power [19–26]. We also show the detail of a stopping power in Sec. II. A three-dimensional computer code is developed for the simulation of a HIB irradiation onto a spherical fuel pellet in direct-driven heavy-ion fusion. The main object of this paper is to clarify a dependence of multi-HIB illumination nonuniformity on parameter values of HIB illumination in HIF. The HIB ions impinge the target surface, penetrate relatively deep into the deposition layer, and deposit their energy in a rather wide region in the deposition layer: this HIB deposition feature influences the beam illumination nonuniformity. The HIB temperature and emittance effects are also evaluated. During the HIB illumination the temperature of the energy deposition layer increases to a few hundred eV. We also investigate the pellet temperature effect on the HIB illumination nonuniformity. We investigate the

*Electronic address: dt030204@cc.utsunomiya-u.ac.jp

†Electronic address: kwt@cc.utsunomiya-u.ac.jp

relationship between a chamber radius and the HIB illumination nonuniformity and study the effect of the total HIB number on the HIB illumination nonuniformity. In an ICF power plant, the position of a fuel pellet may shift from a reactor center, because a pellet may be injected from a pellet injection port at a reactor wall. The HIB illumination nonuniformity may be influenced by a little pellet displacement from the chamber center. In this paper we also investigate the relation between the pellet displacement and the HIB illumination nonuniformity. For the evaluations of the illumination nonuniformity on the target, we compute the root mean square (rms) and the peak to valley (PTV) nonuniformities on the target [27]. In addition, we also perform mode analyses of the HIB deposition energy on the spherical fuel target using the Legendre polynomial and the fast Fourier transfer (FFT).

The simulation results present the fact that the HIB deposition-energy rms nonuniformity on the target is suppressed to a low value, for example, less than 2.0% even by a 32-beam system.

II. SIMULATION MODEL AND CALCULATION METHOD

HIBs may be one of many promising energy-driver candidates in ICF. In this study, we use a lead (Pb^+) beam as a HIB in ICF. The beam parameters are as follows: the mean particle energy is 8.0 GeV, and the maximal initial beam density is $1.3 \times 10^{11} \text{ cm}^{-3}$. The HIB radius varies from 2.7 to 3.8 mm on the pellet surface depending on the beam temperature and emittance. For example, the beam radius is 3.3 mm at the pellet surface in the case of a zero-temperature beam. The chamber radius varies from 2.0 to 8.0 m in our study. In this study, we select three types of beams: the Kapchinskij-Vladimirskij (KV), the semi-Gaussian distribution of a flat constant density in transverse with the Maxwell-distributed particle energy (with 100 MeV beam longitudinal temperature), and the transverse number density in the Gauss distribution with the Maxwell-distributed particle energy (with 100 MeV beam longitudinal temperature). The Gaussian distribution is shown in Eq. (1):

$$n(r_b) = \frac{1}{\sqrt{2\pi}\sigma} \exp\left(-\frac{r_b^2}{2\sigma^2}\right). \quad (1)$$

Here $n(r_b)$ is a number density as a function of beam radius r_b . The σ is standard deviation.

A. Stopping power

The HIB energy deposition comes mainly from the Coulomb collisions between bound and/or free electrons and beam ions. Moreover the Coulomb collisions between beam ions and target ions, nucleus scattering, and the plasma wave excitation contribute the stopping power. We employ the widely used expression of the HIB particle effective charge in Refs. [24–26] and calculate the effective

charge of the HIB particles traveling through the target. The stopping power in the target is considered to be the sum of the energy deposited in a target nuclei, target bound, free electrons, and target ions [22]: $E_{\text{stop}} = E_{\text{nuc}} + E_{\text{free}} + E_{\text{bound}} + E_{\text{ion}}$, where E_{stop} is the deposition energy in the target, E_{nuc} is the deposition energy by the nucleus scattering, E_{free} is by the free electron, and E_{ion} is by the target ion. The nucleus stopping power E_{nuc} becomes effective at the end of the stopping range and describes the elastic Coulomb collisions between the projectile ions and target nuclei [19,28]. When the temperature of the target rises and the target is ionized, free electrons contribute the stopping power, through the Coulomb collisions and the plasma collective wave excitations. The free electron stopping power E_{free} is calculated by the Coulomb collision between projectile ions and the target free electrons [25,26]. E_{ion} is evaluated by the Coulomb collisions between HIB particles and target ions. The Lindhard and the Bethe-Bloch equations describe the bound electron stopping power E_{bound} . We use the Bethe equation to calculate the bound electron stopping power at the high beam energy region in this study [24]. In the middle beam energy region, we calculate the bound stopping power from the Bethe equation with the shell correction [19]. At low beam energies, the stopping power theory is mostly evaluated using the Thomas-Fermi model of the atom [19,20,28,29]. Therefore we use the Lindhard-Scharff-Schiott equation at the low beam energy domain to calculate the bound electron stopping power [19,30].

B. Beam illumination scheme

In this study, we simulate a multi-HIB illumination on the spherical target using 12, 20, 32, 60, 92, and 120-beam irradiation systems. In HIF, the HIB space charge must be neutralized in order to overcome the beam divergence due to the self-space charge. Viable methods of HIB space charge neutralization have already been proposed and studied intensively at the final HIB transport [9,10]. Therefore we assume that HIBs are neutralized perfectly in this paper based on this recent research progress. Each beam position is decided as follows: in the 12-beam system each beam center coincides with the center of each face at the regular dodecahedron. In the same way the 20-beam system is based on the regular icosahedron. We employ the 32-beam system shown by Skupsky [14]. The 60-beam system is vertices of a soccer ball or fullerene [12,13]. The 92-beam system is a combination of 12, 20, and 60-beam systems. The 120-beam system is the combination of two 60-beam systems, each of which is shifted by 90° in the vertex direction.

C. Beam particle orbit in the target

In our study we select two types of targets: one is an Al monolayer pellet structure with a 4 mm external radius as

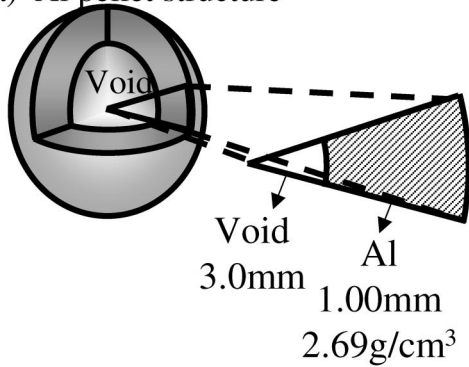
shown in Fig. 1(a) and another one is a Pb + Al pellet structure [7] with the same external radius as shown in Fig. 1(b). In the latter pellet structure, the outer Pb layer thickness and mass density are 0.03 mm and 11.3 g/cm³, respectively. The Al layer thickness and mass density are 0.97 mm and 2.69 g/cm³, respectively. We employ the target temperatures of 1, 100, 200, 300, and 400 eV in this study.

In order to calculate the beam particle orbit we define the beam position at the tangential target surface (R, Θ, Φ) and the focal position (f, Θ_f, Φ_f) as shown in Fig. 2. Then we can calculate the beam particle orbit in the target (r, θ, ϕ) by the following Eq. (2) using the target radius r :

$$\begin{aligned} & \frac{r \sin\theta \cos\phi - R \sin(\Theta) \cos(\Phi)}{f \sin(\Theta_f) \cos(\Phi_f) - R \sin(\Theta) \cos(\Phi)} \\ &= \frac{r \sin\theta \sin\phi - R \sin(\Theta) \sin(\Phi)}{f \sin(\Theta_f) \sin(\Phi_f) - R \sin(\Theta) \sin(\Phi)} \\ &= \frac{r \cos\theta - R \cos(\Theta)}{f \cos(\Theta_f) - R \cos(\Theta)}. \end{aligned} \quad (2)$$

From Eq. (2), we calculate the beam orbit, i.e., (r, θ, ϕ) by

(a) Al pellet structure



(b) Pb+Al pellet structure

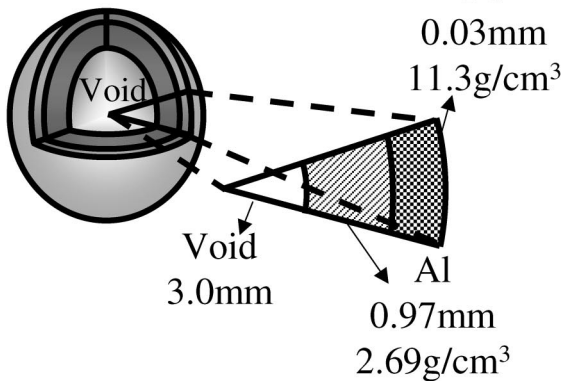


FIG. 1. Fuel target structure. (a) The Al layer thickness and mass density are 1.00 mm and 2.69 g/cm³. (b) The Pb layer thickness and mass density are 0.03 mm, 11.3 g/cm³ and Al are 0.97 mm, 2.69 g/cm³, respectively. The initial target temperature varies from 1 to 400 eV in this study.

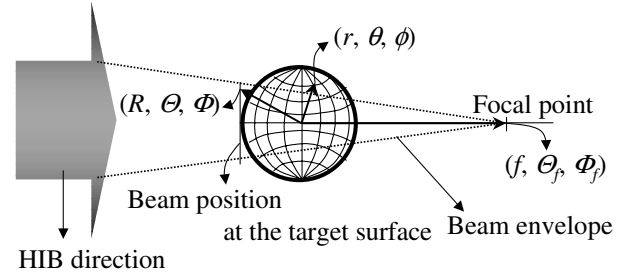


FIG. 2. Beam focal spot and the target. (R, Θ, Φ) means the beam position at the tangential target surface, (f, Θ_f, Φ_f) is the focal position, and (r, θ, ϕ) is the beam particle orbit in the target.

the known values of the beam position (R, Θ, Φ) , the focal position (f, Θ_f, Φ_f) , and the value of the target radius r .

D. Beam divergence

The beam particle may slightly diverge by a finite emittance in the transverse direction. Therefore we include a beam emittance effect and change the beam radius not to miss the target so that all ions hit the target surface. In Fig. 3, we define a relation between a beam transverse emittance and a divergence angle α_{dvr} . R_{en} is the beam radius at the fusion reactor wall, R_{ch} is the reactor radius, f is the focal length between the beam focal position and the target center, R_f is the focal spot radius, R_p is the pellet radius, and R_{beam} is the beam radius at the target surface (see Fig. 3). The beam divergence angle α_{dvr} is defined as follows:

$$\alpha_{\text{dvr}} = \frac{\varepsilon_r}{R_{\text{en}}}. \quad (3)$$

Here, ε_r is a beam transverse emittance:

$$R_f = (R_{\text{ch}} + f) \tan(\alpha_{\text{dvr}}). \quad (4)$$

In this study, we calculate a beam divergence angle from the beam transverse emittance ε_r . We change the beam transverse emittance from 2.0 to 10 mm mrad in this study in order to know the emittance influence. From Eq. (3), the beam divergence angle α_{dvr} is calculated to be about $8.2 \times 10^{-3}^\circ$ in the case of $\varepsilon_r = 5.0$ mm mrad and $R_{\text{en}} = 35$ mm. In our study the relation between the focal length f and the beam radius R_{beam} is defined by

$$f = \frac{R_{\text{beam}} \cdot R_{\text{ch}} - R_p \cdot R_{\text{en}}}{R_{\text{en}} - R_{\text{beam}}}. \quad (5)$$

In addition, the beam focal position moves backward and forward by the beam divergence angle as shown in Fig. 3. Therefore we use Eqs. (3) and (5) in order to calculate backward and forward focal positions:

$$\begin{aligned} f_{\text{min}} &= R_{\text{en}} \cdot \tan(\xi - 0.01745\alpha_{\text{dvr}}) - R_{\text{ch}}, \\ f_{\text{max}} &= R_{\text{en}} \cdot \tan(\xi + 0.01745\alpha_{\text{dvr}}) - R_{\text{ch}}. \end{aligned} \quad (6)$$

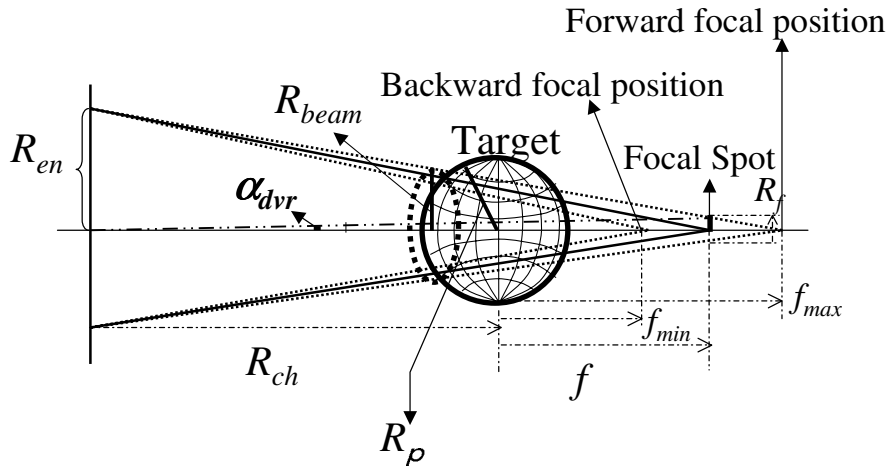


FIG. 3. The relationship between a beam emittance and the divergence angle at the beam port. R_{en} is the chamber radius in the fusion reactor, R_{ch} is the reactor radius, f is the beam focal spot, R_f is the focal spot radius, R_p is the pellet radius, α_{dvr} is the beam divergence angle, and R_{beam} is the beam radius in front of the target.

Here f_{min} is the backward focal position of the beam focal spot, f_{max} is the forward focal position (see Fig. 3), and ξ is given by $\xi = \tan^{-1}[(R_{ch} + f)/R_{en}]$. Based on Eqs. (5) and (6), the beam radius at the fuel pellet surface changes between 2.7 and 3.8 mm in the case of 5.0 mm mrad emittance, so that any HIB ions do not miss impinging the pellet surface.

E. Deposition-energy calculation procedure

In this study, we divide one HIB into 316 beamlets in order to simulate a precise HIB illumination nonuniformity as shown in Fig. 4(a). Each beamlet deposits its energy on space meshes of the spherical target as shown in Fig. 4(b). Then in order to calculate the deposition energy of one HIB in one mesh, we use Eq. (7):

$$E_{stop} = \frac{dE}{dl} \cdot V \cdot n^{2/3}. \tag{7}$$

Here dE/dl is the stopping power, that is, a beamlet deposition energy per unit length, n is the beam particle number density, and V is the volume of one cell in the target.

The deposition energy is distributed to the mesh points. Each beamlet has an effective area, and the deposition energy is distributed to the meshes by the beamlet effective area as shown in Fig. 4(b). When multi-HIBs illuminate the spherical target and deposit their energy on the target, the deposition energy is calculated by Eq. (8),

$$E_{ijk} = \sum_N E_{stop}. \tag{8}$$

Here E_{ijk} is the deposition energy at each mesh point denoted by (i, j, k) in the 3-dimensional space and N is the number of HIBs impinging the cell.

F. Evaluation of nonuniformity on the spherical target

In our study, we evaluate the energy nonuniformity at the target. In ICF, the beam irradiation nonuniformity on the fuel target must be suppressed under a few percent in

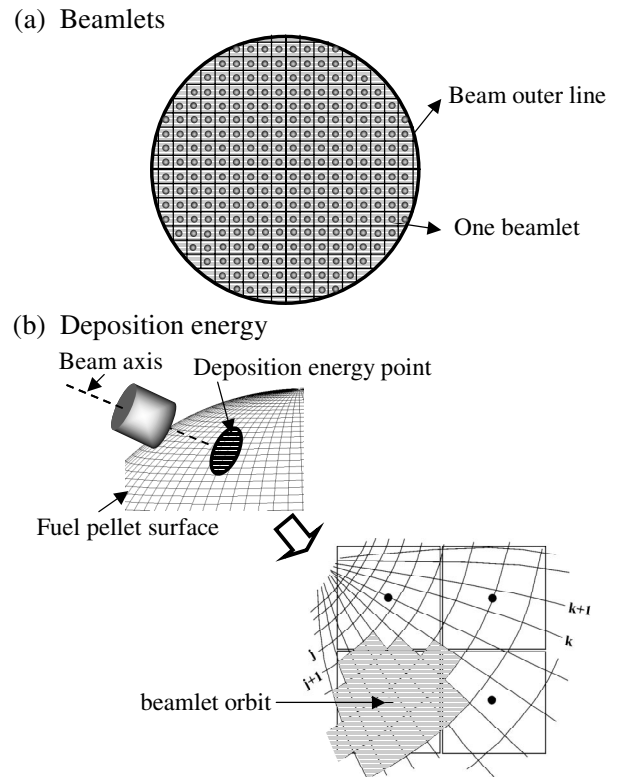


FIG. 4. (a) Beamlet. Each beamlet deposits its energy in the spherical target, then the deposition energy is divided into mesh points on the spherical target. (b) Deposition energy at each mesh point. The beamlets have an effective area. The deposition energy at a mesh point is defined from the beamlet effective area.

order to achieve a symmetric fuel pellet implosion [7,12–17]. In HIB-ICF the Bragg peak deposition area plays the most important role for a target implosion. Therefore we define the total relative rms and PTV nonuniformity as follows:

$$\sigma_{\text{rms}} = \sum_i^{n_r} w_i \sigma_{\text{rms}i}, \quad (9)$$

$$\sigma_{\text{rms}i} = \frac{1}{\langle E \rangle_i} \sqrt{\frac{\sum_j \sum_k (\langle E \rangle_i - E_{ijk})^2}{n_\theta n_\phi}}, \quad w_i = \frac{E_i}{E},$$

$$\sigma_{\text{PTV}} = \sum_i^{n_r} w_i \sigma_{\text{PTV}i}, \quad \sigma_{\text{PTV}i} = \frac{E_i^{\text{max}} - E_i^{\text{min}}}{2\langle E \rangle_i}. \quad (10)$$

Here σ_{rms} and σ_{PTV} are the rms and PTV nonuniformities, respectively. $\sigma_{\text{rms}i}$ and $\sigma_{\text{PTV}i}$ are the rms and PTV nonuniformities on the i th ($r = \text{const}$) surface of deposition, respectively. w_i is the weight function in order to include the Bragg peak effect or the deposition profile. n_r , n_θ , and n_ϕ are mesh numbers in each direction of the spherical coordinate. $\langle E \rangle_i$ is the mean deposition energy on the i th surface, E_i is the total deposition energy on the i th surface, and E is the total deposition energy. E_i^{max} and E_i^{min} are the maximal and minimal deposition energies on the i th surface, respectively.

We also performed mode analyses on the spherical fuel target by using the spherical harmonic function $Y_n^m(\theta, \phi)$:

$$s_n^m = \frac{1}{4\pi} \int_0^\pi \sin\theta d\theta \int_0^{2\pi} E(\theta, \phi) Y_n^m(\theta, \phi) d\phi. \quad (11)$$

Here s_n^m is an amplitude of energy spectrum, n and m are the mode numbers, and θ and ϕ are azimuthal and vertex angles, respectively. $E(\theta, \phi)$ is the deposition energy from the beam particles at each mesh point. By using the Legendre polynomial function $P_n^m(\cos\theta)$, the spherical harmonic function is described as follows:

$$Y_n^m(\theta, \phi) = P_n^m(\cos\theta) e^{im\phi}. \quad (12)$$

Therefore the spectrum of the deposition energy on a spherical target is

$$s_n^m = \frac{1}{4\pi} \int_{-1}^1 d(\cos\theta) \int_0^{2\pi} E(\theta, \phi) P_n^m(\cos\theta) e^{-im\phi} d\phi. \quad (13)$$

In order to compute the energy spectrum s_n^m on a computer, Eq. (13) is modified by using the Gauss-Legendre integration and FFT as follows:

$$s_n^m = \frac{1}{2} \sum_{j=1}^J g_j F^m(\theta_j) P_n(\cos\theta_j), \quad (14)$$

where

$$F^m(\theta_j) = \frac{1}{K} \sum_{k=0}^{K-1} E(\theta_j, \phi_k) e^{-im\phi_k}. \quad (15)$$

Here g_j is the Gaussian weight corresponding to the zero points, and J is the number of zero points. In our study, the Gaussian weight is given by Eq. (16):

$$g_j = \frac{2}{(1 - \cos^2\theta_j) \{P'_N(\cos\theta_j)\}^2}. \quad (16)$$

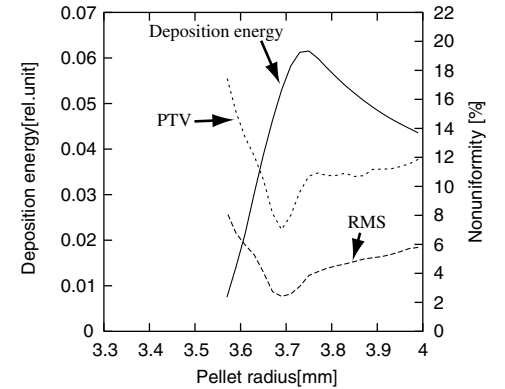
Here $P'_N(\cos\theta_j)$ is the Legendre polynomial differential coefficient. K is a mesh number in the vertex direction. In order to include the Bragg peak effect we calculate the spectrum of the deposition energy at the Bragg peak layer and we also calculate the global energy spectrum using the weight function w_i . The summation of the energy-spectrum amplitude is normalized to be 1.0 in our study.

III. SIMULATION RESULTS

A. Deposition nonuniformity

Figure 5(a) shows the deposition energy of beam particles at each surface without the beam temperature effect for the Al layer target with the chamber radius of 5 m, 120-beam system, and the KV distribution. In Fig. 5(a),

(a) Without beam temperature



(b) With beam temperature

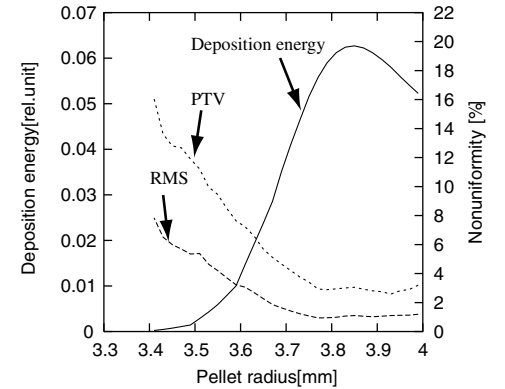


FIG. 5. The deposition energy of beam particles in the relative unit and nonuniformities at each surface in the cases (a) without the beam temperature effect and (b) with the temperature effect for the Al layer target for the chamber radius of 5 m, 120-beam system, and the semi-Gaussian distribution.

we can see the Bragg peak at the middle layer of the energy absorption region, and the rms and PTV nonuniformities are low at the Bragg peak layer. At the end of the beam particle stopping region, the deposition energy is much smaller compared to the Bragg-peak-layer's one. In actual the pressure peak generated by the HIBs deposition at the Bragg peak region drives the inner fuel to the implosion with a high speed (typically $\sim 3 \times 10^7$ cm/s). Based on this reason and on results of the implosion studies previously performed [7,9,15,25,26], it is known that the HIBs deposition energy in the Bragg peak region contributes mainly to the implosion. Therefore, in this paper, we calculated total rms nonuniformity using the weight function w_i in order to include the Bragg peak effect. The rms nonuniformity is evaluated by Eq. (9), and the result is $\sigma_{\text{rms}} = 4.44\%$. Figure 5(b) shows the energy deposition in the case of a 120-beam system, 5 m chamber radius, the semi-Gaussian distribution, and the Al target including the longitudinal beam temperature of 100 MeV and the transverse beam radial emittance of 5.0 mm mrad. In Fig. 5 we can see that the Bragg peak moves slightly outward in the radial direction and the rms nonuniformity becomes $\sigma_{\text{rms}} = 1.52\%$. The HIB illumination nonuniformity in the realistic case including the beam temperature or the beam divergence becomes small

compared with that in the case with the zero-temperature HIB. This result presents the fact that the HIB illumination nonuniformity can be smoothed and suppressed due to the beam temperature or the transverse emittance.

We also calculate the deposition-energy spectra at the Bragg peak layer for the zero-temperature beam ($r = 3.73$ mm) and for the case with the beam temperature of 100 MeV ($r = 3.83$ mm) as shown in Figs. 6(a) and 6(b). Figures 6(c) and 6(d) are the global nonuniformity spectra using the weight w_i for the zero-temperature beam and for the case with the beam temperature of 100 MeV. In Fig. 6, (n, m) and s_n^m are the mode numbers and the amplitude of the spectrum, respectively. If the deposition energy is distributed in complete spherically symmetric, the amplitude of spectrum is set to 1.0 in the mode $(n, m) = (0, 0)$ in our study. In order to achieve a symmetric energy deposition in the direct-drive HIB-ICF, most spectrums should be concentrated on the mode $(n, m) = (0, 0)$, and the amplitude of the mode $(n, m) = (0, 0)$ has a large value near 1.0 in our simulation results, compared with those for other modes. For this reason, in this paper, we focus on the amplitudes of spectrum modes except the mode $(n, m) = (0, 0)$. Therefore our calculation results shown in spectrum figures present the spectrum without the mode of $(n, m) =$

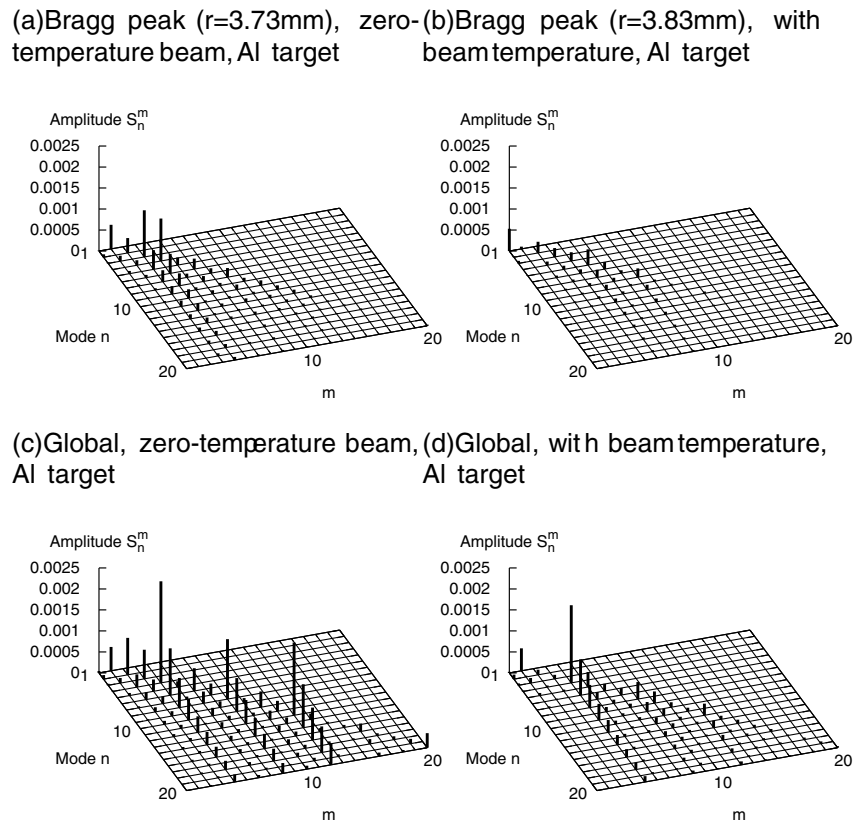


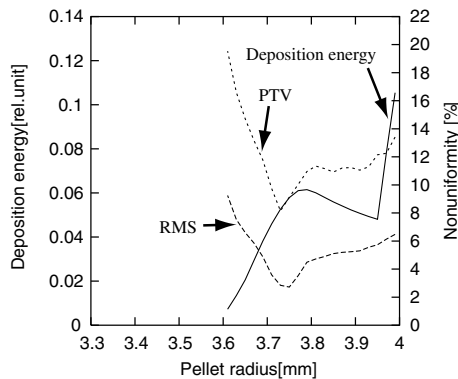
FIG. 6. The energy spectra at the Bragg peak layer (a) for the zero-temperature beam ($r = 3.73$ mm) and (b) with the beam temperature ($r = 3.83$ mm) for the Al layer target. The global nonuniformity spectra using the weight w_i for the (c) zero-temperature beam and (d) with the beam temperature for the Al layer target.

(0, 0). In Fig. 6 the amplitude of the spectra in the case of the Bragg peak layer is small compared with that for the global nonuniformity. This result means that the deposition energy at the Bragg peak layer is more uniform compared with the deposition energies at other layers. This is also confirmed by the results in Fig. 5. In HIB-ICF the Bragg peak area plays an important role for the symmetric target implosion. Therefore we expect that we may realize an effective compression of target and efficient target implosion. We also confirm that the amplitude in the case including the beam temperature becomes small compared with that in the case of the zero beam temperature, as expected by the results presented above. Moreover in Figs. 6(a) and 6(b) the amplitude of the deposition-energy spectrum at the mode $(n, m) = (0, 0)$ is 0.97 in the case with the zero beam temperature, and the amplitude of the energy spectrum at the mode $(n, m) = (0, 0)$ is 0.99 in the case including the beam temperature.

Figure 7 shows the energy deposition in the target in the case of Pb + Al layers target structure (a) without the beam temperature (KV) and (b) with the beam tempera-

ture of 100 MeV and the transverse beam emittance of 5.0 mm mrad. The number of HIBs is 120, the chamber radius is 5 m, and particle number density is in the semi-Gaussian distribution in both cases. The HIB energy is deposited in the Al energy-absorber layer as well as the Pb layer. However the energy deposited in the Al pusher/energy-absorption layer in our study is used effectively for the fuel implosion [7]. The Pb layer behaves as a tamper. In this type of HIF pellet the thickness of the Al pusher layer is designed to be sufficiently thick so that a perturbation of the Pb tamper layer cannot reach the fuel during the HIB pulse duration and at the same time HIB particles do not reach the fuel in order to prevent a fuel preheating. Therefore the HIB energy deposition nonuniformity is evaluated only in the Al layer in this study. In these cases, the rms nonuniformity is $\sigma_{\text{rms}} = 1.72\%$ for the case including the beam temperature of 100 MeV, and $\sigma_{\text{rms}} = 5.25\%$ for the case with the zero beam temperature. We also calculate the spectra as shown in Figs. 8: (a) in the case with the zero beam temperature at the Bragg peak layer ($r = 3.79$ mm), (b) with the 100 MeV beam temperature at the Bragg peak layer ($r = 3.87$ mm), (c) the global nonuniformity in the case with the zero-temperature beam, and (d) the global nonuniformity with the 100 MeV beam temperature. In Fig. 8, the amplitude of the energy spectra at the Bragg peak layer is small compared with that for the global nonuniformity. We also confirm that the amplitude in the case with the beam temperature of 100 MeV and the 5.0 mm mrad transverse emittance is small compared with that in the case with the zero beam temperature. From these results, we found that the Pb tamper effect is minor. The energy-spectrum value is 0.99 at the mode $(n, m) = (0, 0)$ in the case including the beam temperature and 0.96 at the mode $(n, m) = (0, 0)$ in the case with the zero beam temperature. The rms nonuniformity in the case of Pb + Al target is 1.72%, and this result also shows a good result for a symmetric energy deposition (see Fig. 9).

(a) Without beam temperature



(b) With beam temperature

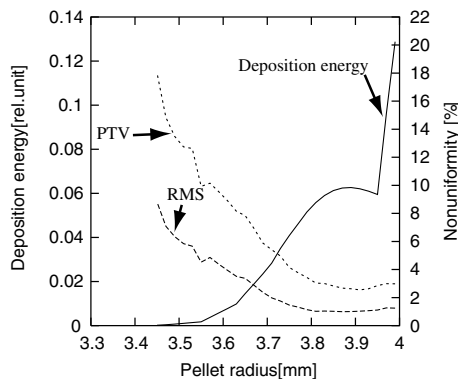
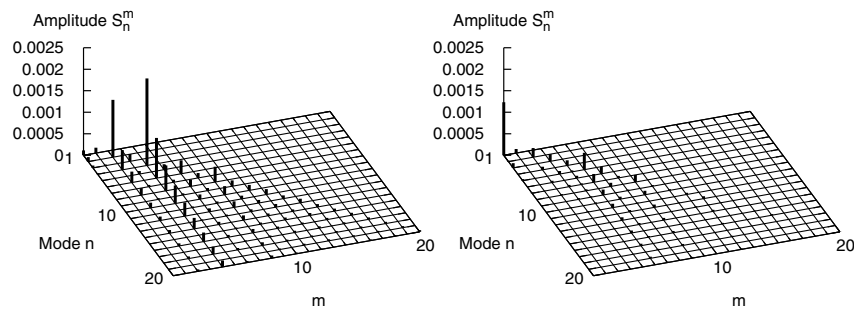


FIG. 7. The deposition energy of beam particles in the relative unit and nonuniformities at each surface in the cases (a) without the beam temperature effect and (b) with the temperature effect for the Pb + Al layer target for the chamber radius of 5 m, 120-beam system, and the semi-Gaussian distribution.

B. Chamber radius effect

Figure 10 shows a relationship between the HIB-ICF reactor chamber radius R_{ch} and the HIB illumination nonuniformity for the Al layer target with the beam temperature and the semi-Gaussian distribution in the cases of 32, 60, and 120-beam systems. In this case we fix the beam transverse emittance to 5.0 mm mrad and vary the focal spot radius R_f and distance f . The rms nonuniformity changes gradually along with the change in the reactor chamber radius. In recent ICF designs, the chamber radius of the fusion power plant is about 4.0–6.0 m [2,8]. In our results the optimal nonuniformity stays at around the 3.0–6.0 m chamber radius in the 32, 60, and 120-beam systems for the fixed emittance of 5.0 mm mrad. These results present the fact that the rms

(a)Bragg peak ($r=3.79\text{mm}$), zero- (b)Bragg peak ($r=3.87\text{mm}$), with temperature beam, Pb+Al target beam temperature, Pb+Al target



(c)Global, zero-temperature beam, (d)Global, with beam temperature, Pb+Al target Pb+Al target

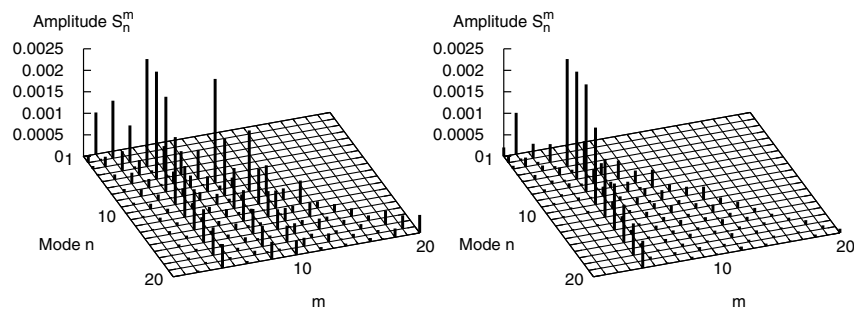


FIG. 8. The energy spectra at the Bragg peak layer (a) for the zero-temperature beam ($r = 3.79 \text{ mm}$) and (b) with the beam temperature ($r = 3.87 \text{ mm}$) for the Pb + Al layer target. The global nonuniformity spectra using the weight w_i for the (c) zero-temperature beam and (d) with the beam temperature for the Pb + Al layer target.

nonuniformity is kept low enough even in the 32-beam system in the cases with a realistic ICF reactor chamber radius. We also perform another parameter study to demonstrate a requirement for the emittance in order to

realize the low nonuniformity when the chamber radius varies. In this study we fix $R_p = 4 \text{ mm}$ and $R_f = 0.66 \text{ mm}$ and change the chamber radius R_{ch} . By Eqs. (3) and (4) the emittance is computed as shown in Fig. 11. In this parameter study the nonuniformity is kept small (see

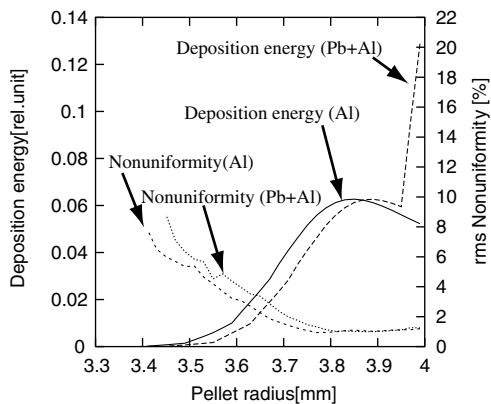


FIG. 9. The deposition energy of beam particles in the relative unit and rms nonuniformity at each surface in the case with the temperature effect for the Al and the Pb + Al layer targets for the chamber radius of 5 m, 120-beam system, and the semi-Gaussian distribution.

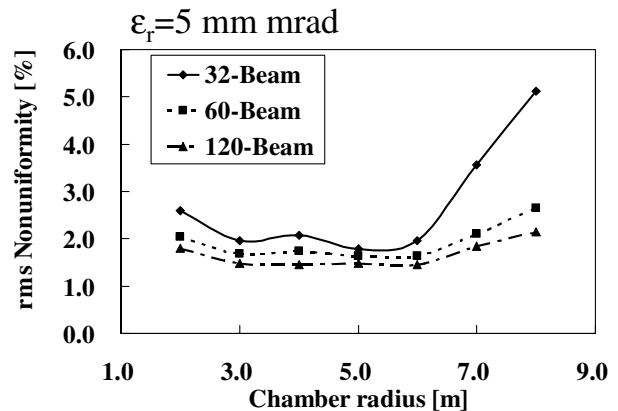


FIG. 10. The chamber radius versus the rms nonuniformity in the cases of the Al layer target with the semi-Gaussian distribution including the beam temperatures for the 32, 60, and 120-beam systems.

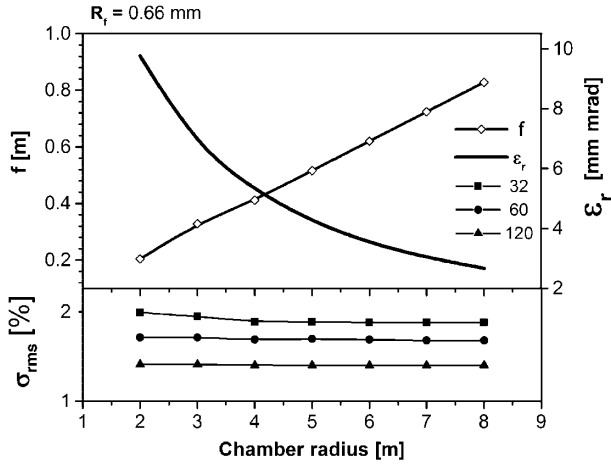


FIG. 11. The relationship between the beam transverse emittance, focal distance, and the rms nonuniformity. The beam emittance should decrease and the focal distance f should increase with the increase in the chamber radius R_{ch} .

σ_{rms} in Fig. 11), though the requirement for the emittance becomes severe with the increase in the chamber radius R_{ch} . These results present the fact that the HIB accelerator should deliver HIBs with a low beam transverse emittance and that we should select the chamber radius.

C. The Gaussian beam

We use the Gaussian distribution in order to simulate a more realistic case compared with the semi-Gaussian distribution as the beam particle transverse number density distribution. We optimize the standard deviation σ for any beam systems in order to suppress the beam irradiation nonuniformity. Figure 12 shows the Gaussian distributions with the various standard deviations σ selected as

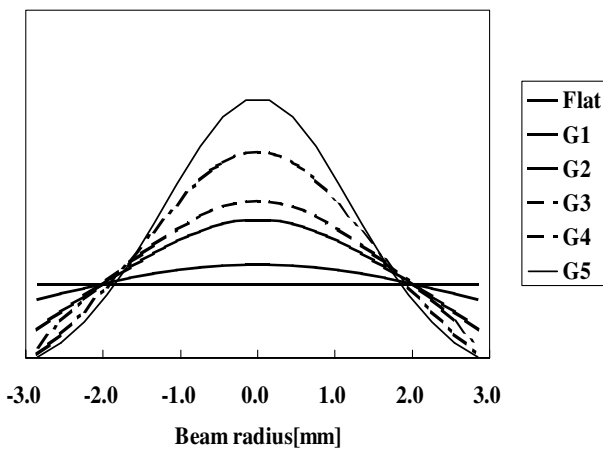


FIG. 12. The Gaussian distribution. The standard deviation σ of the Gaussian distribution is defined as follows. G1: $\sigma = 1.20R_{beam}$; G2: $\sigma = 1.00R_{beam}$; G3: $\sigma = 0.80R_{beam}$; G4: $\sigma = 0.55R_{beam}$; G5: $\sigma = 0.50R_{beam}$.

follows: $\sigma = 1.20R_{beam}$ (we call this type “G1” in this study), $\sigma = 1.00R_{beam}$ (G2), $\sigma = 0.80R_{beam}$ (G3), $\sigma = 0.55R_{beam}$ (G4), and $\sigma = 0.50R_{beam}$ (G5). Figure 13 shows the relation between the rms nonuniformity, the Gaussian types, and the beam numbers for the various σ in the case of the Al layer target with the chamber radius of 5 m including the longitudinal beam temperature of 100 MeV and the transverse beam radial emittance of 5.0 mm mrad. In Fig. 13 we confirm that the nonuniformities are suppressed low in the cases of G1–G3 for the larger number of beams (> 32). This result shows that the sharp Gaussian distribution should be avoided.

D. Beam number effect

Figure 14 shows the rms nonuniformity versus the HIB total number in the cases of (a) Al and (b) Pb + Al layer targets with the chamber radius of 5 m. The marked diamonds, triangles, squares, and crosses mean the results in the cases of the Gaussian distribution (G2) with and without the temperature effect and of the semi-Gaussian distribution with and without the temperature effect, respectively. Particularly, in the case with the Gaussian distribution with the beam temperature of 100 MeV marked by diamonds in Fig. 14, the rms nonuniformity in the case of the 120-beam system is 1.49% for the Al structure and 1.60% for the Pb + Al structure. These values are close to the values in the semi-Gaussian distribution with the beam temperature: 1.52% for the Al structure and 1.72% for the Pb + Al structure in the case of the 120-beam system for the semi-Gaussian with the beam temperature. Therefore our calculation results also demonstrate that the realistic Gaussian beam is good for HIB-ICF in order to achieve a symmetric implosion.

E. Target temperature effect

The target temperature increases in HIB-ICF, when HIBs impinge on a fuel pellet. When the target temperature increases, the beam particle stopping range changes with a target temperature [21,22]. When the stopping range changes, the nonuniformity of the deposition energy at the target may change. Therefore we should investigate the relationship between the deposition-energy nonuniformity and the target temperature. From Fig. 15(a) we can confirm that the beam particle stopping range changes with a target temperature change. Figure 15(b) shows the target temperature versus the rms nonuniformity. We use the Al layer target and the semi-Gaussian beam including the longitudinal beam temperature of 100 MeV and the transverse beam radial emittance of 5.0 mm mrad in the cases of 32, 60, and 120-beam systems. When the target temperature increases, the rms nonuniformity does not change much in the target temperature range expected in HIB-ICF. This result demonstrates that the HIB illumination nonuniformity is kept

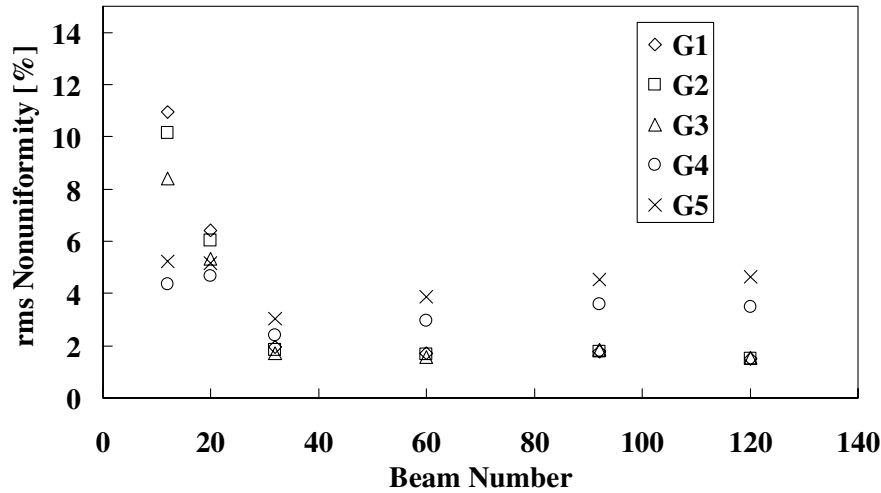


FIG. 13. The rms nonuniformity versus HIB total number in the case of the Al layer target with the chamber radius of 5 m including the longitudinal beam temperature of 100 MeV and the transverse beam radial emittance of 5.0 mm mrad using five Gaussian types.

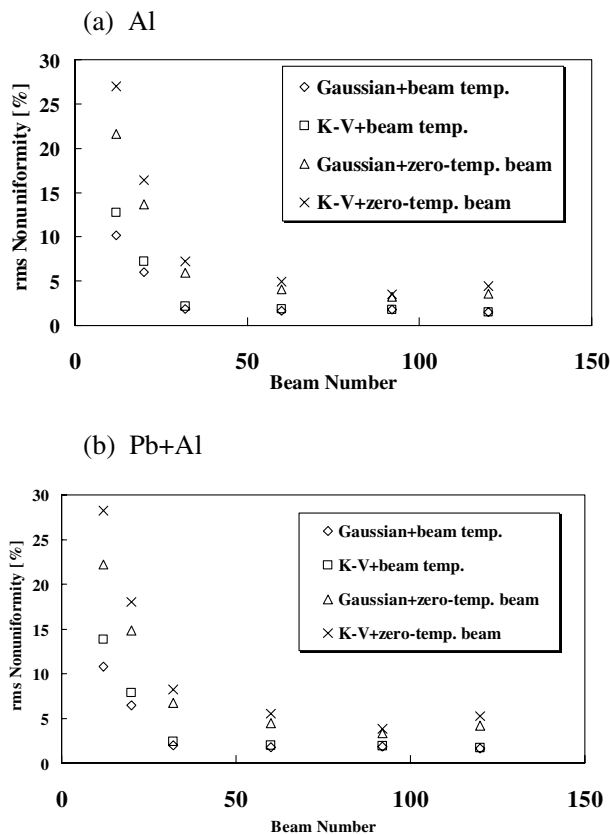


FIG. 14. The rms nonuniformity versus the HIB total number in the cases of (a) the Al layer target and (b) the Pb + Al layer target with the chamber radius of 5 m. The marked diamonds, triangles, squares, and crosses mean the results in the cases of the Gauss distribution (G2) with and without the temperature effect, and of the semi-Gaussian distribution with and without the temperature effect, respectively.

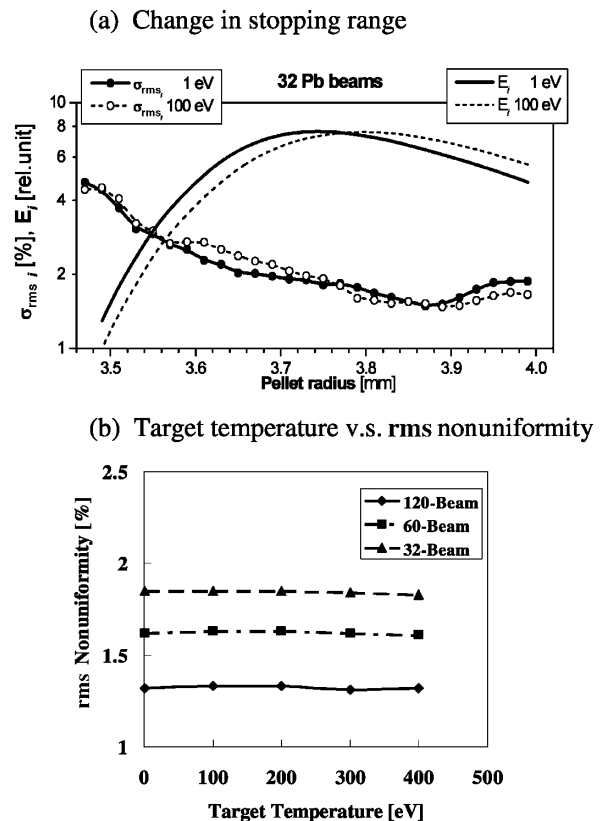


FIG. 15. (a) The deposition energy of beam particles and rms nonuniformity at each surface in the case with the beam temperature effect and target temperature (1 and 100 eV) for the Al layer target, the chamber radius of 5 m, 32-beam system, and the semi-Gaussian distribution. (b) The rms nonuniformity versus the target temperature.

low during the HIB pulse duration, once the HIB illumination pattern is selected for the cold target.

F. Displacement of fuel pellet position in a reactor

In the above subsections, all calculations were performed with the assumption that a pellet is set just to the chamber center. Such a requirement is difficult to be realized in practice. Therefore a little pellet displacement from the reactor chamber center is evaluated in this subsection. We assume that the pellet is injected into the chamber vertically and simulate the effect of a little displacement dz as shown in Fig. 16(a). Our illumination pattern is a basic spherically symmetric pattern. So the vertical displacement of dz may be sufficiently general for our present purpose. The results for the HIB irradiation systems investigated are plotted in Fig. 16 in the cases of the Al layer target, the Gaussian beam (G2) including the beam temperature with the chamber radius of (b) 2 m and (c) 5 m. In Figs. 16(b) and 16(c) we can confirm that the

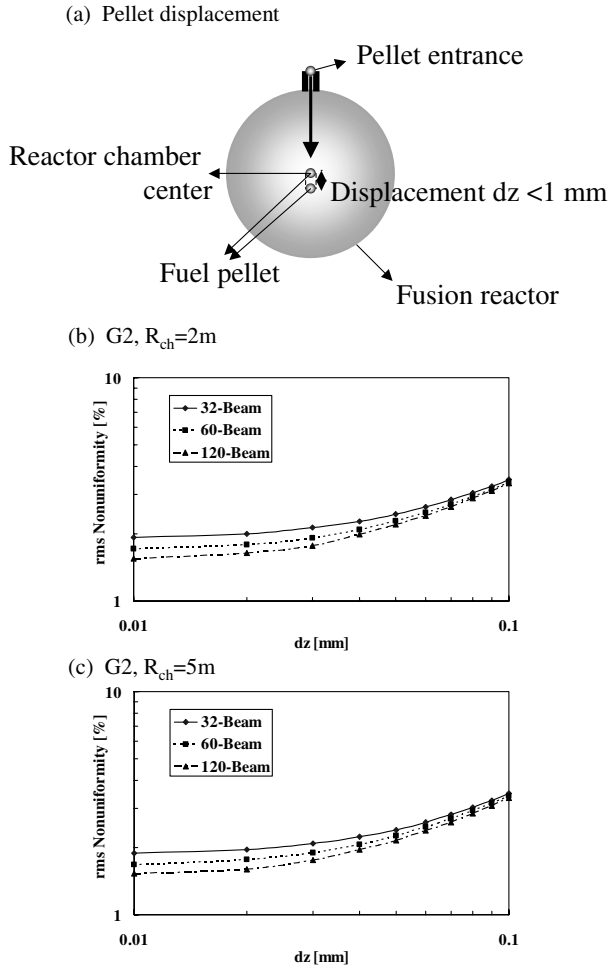


FIG. 16. (a) Pellet displacement from the chamber center. The pellet displacement versus the rms nonuniformity for the chamber radius of (b) 2 m and (c) 5 m in the cases of 32, 60, and 120-beam systems.

HIB irradiation nonuniformity is sensitive to the pellet position displacement in both cases. This result means that the pellet displacement may be a serious problem in HIB-ICF.

IV. DISCUSSIONS AND CONCLUSIONS

In HIF the HIB nonuniformity induces the pressure or acceleration nonuniformity and consequently induces the implosion and ρR nonuniformities. Here we discuss the relation between the HIB nonuniformity and the implosion radial acceleration nonuniformity following Ref. [31]: in [31] Sacks *et al.* also present an estimation of the HIB irradiation nonuniformity, as well as a discussion on a relation between an implosion nonuniformity and the HIB irradiation nonuniformity and suggest a pressure smoothing effect. First we define the radial acceleration nonuniformity $\delta a / \langle a \rangle$ as a summation of a ratio between the average acceleration $\langle a \rangle_i$ at the i th surface and the variation of acceleration δa_i along the i th surface, including the weight function w_i [see Eq. (9)]. The HIB energy deposition nonuniformity consisted of mainly the variation of the HIB deposition-energy amount and the variation of the deposition position [31]; in our study the former factor is evaluated through δa_i and w_i represents the latter. The pressure in one cell at the deposition layer is estimated by $E_{ijk} / \delta V_{ijk}$. Here δV_{ijk} is the volume of one cell. Therefore we can estimate the radial acceleration a_{ijk} at each mesh point as follows:

$$a_{ijk} \propto \frac{E_{ijk}}{\delta V_{ijk} \cdot \lambda_{ijk}}. \quad (17)$$

Here λ_{ijk} is a scale length of the pressure gradient at each mesh point. Moreover the mean radial acceleration $\langle a \rangle_i$ at the i th surface is given by

$$\langle a \rangle_i \propto \frac{\langle E \rangle_i}{\langle \delta V \rangle_i \cdot \lambda_i}. \quad (18)$$

Here $\langle \delta V \rangle_i$ is the mean volume of each cell and λ_i is the mean scale length of the pressure gradient at the i th surface.

In our study, we estimate the variation of radial acceleration at the i th surface using the rms as follows:

$$\delta a_i \propto \frac{\sqrt{\sum_j \sum_k (\langle a \rangle_i - a_{ijk})^2}}{n_\theta n_\phi}. \quad (19)$$

From Eqs. (17)–(19), we can calculate the radial acceleration nonuniformity as follows:

$$\begin{aligned}
\frac{\delta a}{\langle a \rangle} &= \sum_i w_i \cdot \frac{\delta a_i}{\langle a \rangle_i} \\
&= \sum_i w_i \cdot \frac{\sqrt{\sum_j \sum_k \left(\frac{\langle E \rangle_i}{\langle \delta V \rangle_i \cdot \lambda_i} - \frac{E_{ijk}}{\delta V_{ijk} \cdot \lambda_{ijk}} \right)^2} / n_\theta n_\phi}{\frac{\langle E \rangle_i}{\langle \delta V \rangle_i \cdot \lambda_i}} \\
&= \sum_i w_i \cdot \sqrt{\sum_j \sum_k \left(\frac{\langle E \rangle_i}{\langle \delta V \rangle_i \cdot \lambda_i} - \frac{E_{ijk}}{\delta V_{ijk} \cdot \lambda_{ijk}} \right)^2} \cdot \frac{1}{n_\theta n_\phi}. \quad (20)
\end{aligned}$$

In an actual fuel target we can usually assume $\delta V_{ijk} \approx \langle \delta V \rangle_i$ and $\lambda_i \approx \lambda_{ijk}$ at each i th surface. Therefore we can rewrite Eq. (20) as follows:

$$\frac{\delta a}{\langle a \rangle} \approx \sum_i w_i \cdot \sqrt{\sum_j \sum_k \left(\frac{\langle E \rangle_i - E_{ijk}}{\langle E \rangle_i} \right)^2} \cdot \frac{1}{n_\theta n_\phi} = \sigma_{\text{rms}}. \quad (21)$$

Equation (21) shows that the global acceleration nonuniformity can be estimated by the rms deposition-energy nonuniformity [see Eq. (9)]. Therefore the results presented in this paper serve important information in the HIF direct-driven pellet implosion.

In this paper, we studied the HIB deposition nonuniformity in a direct-driven HIB-ICF pellet. For various beam parameters and different reactor chamber radii we investigated the deposition-energy nonuniformity using 12, 20, 32, 60, 92, and 120-beam irradiation systems. The HIB diverges slightly by the beam temperature. We include the effect of a beam longitudinal temperature and the beam transverse emittance. In our simulation results we confirm that the HIB illumination nonuniformity is $\sigma_{\text{rms}} = 1.52\%$ in the case of the Al monolayer structure target, the beam temperature of 100 MeV, the 120-beam system, and the semi-Gaussian particle density distribution. In the case of the Pb + Al target structure, $\sigma_{\text{rms}} = 1.72\%$. On the other hand, the rms nonuniformity using the Gaussian beam including the beam temperature is close to the nonuniformity for the semi-Gaussian distribution with the temperature effect ($\sigma_{\text{rms}} = 1.49\%$ for the Al layer, $\sigma_{\text{rms}} = 1.60\%$ for the Pb + Al layer). From these results, we expect that the fuel can be successfully imploded and the fusion energy can be released from a direct-driven fuel pellet in HIB-ICF using the Gaussian or semi-Gaussian HIBs. Moreover we analyzed the spectrum of the HIB illumination nonuniformity in the spherical target. As a result, the deposition-energy nonuniformity in the target includes higher modes with sufficiently low amplitudes. Therefore the mode analyses also demonstrate that by using an appropriate illumination pattern and the selected HIB illumination parameter values the sufficiently low nonuniformity can be realized. From the relationship between the chamber radius and the HIB illumination nonuniformity in the cases of 32, 60, and 120-beam systems, with the beam temperature and

the semi-Gaussian distribution particle number density, the rms nonuniformity does not change much with the change in the reactor chamber radius as shown in Fig. 10 at a realistic chamber radius R_{ch} of about 3–6 m. In this parameter range of R_{ch} we can expect that the HIB illumination nonuniformity is suppressed less than a few percent. We also demonstrated the important effect of the HIB transverse emittance in Fig. 11. The results show that the beam transverse emittance should be sufficiently low and that the reactor chamber radius should be optimized.

In HIB-ICF, the target temperature increases during the HIB pulse duration. Therefore we also calculated the relationship between the target temperature and the HIB illumination nonuniformity. We found that even if the target temperature increases in a typical temperature range in HIB-ICF, the rms nonuniformity does not change much. This result presents the fact that the rms nonuniformity is kept low during the HIB pulse illumination onto a direct-driven pellet in ICF. Moreover we investigated the nonuniformity growth due to the small pellet displacement of the pellet position from the chamber center. The calculation results demonstrated that the pellet displacement is a serious problem in HIF. In order to investigate a dynamic HIB illumination nonuniformity, hydrodynamic implosion simulations coupled with our 3D HIB illumination code should be performed, and this work should be done in the near future as the next step.

ACKNOWLEDGMENTS

This work is partly supported by the JSPS (Japan Society for the Promotion of Science). The authors would like to thank the HIF research group at VNL, USA, Professor T. Katayama, Professor M. Ogawa, Professor K. Horioka, and our colleagues in a HIF research group in Japan, Dr. M. Murakami, Professor K. Mima, Professor K. Tachibana, and Professor A. B. Blagoev for their fruitful discussions on this subject.

-
- [1] J. D. Lindl, R. W. Mccrory, and M. Campbell, *Phys. Today* **45**, No. 9, 32 (1992).
 - [2] W. J. Hogan, R. Bangerter, and G. L. Kulcinski, *Phys. Today* **42**, No. 9, 42 (1992).
 - [3] M. Tabak and D. Callahan-Miller, *Phys. Plasmas* **5**, 1895 (1998).
 - [4] M. Tabak and D. Callahan-Miller, *Nucl. Instrum. Methods Phys. Res., Sect. A* **415**, 75 (1998).
 - [5] M. Tabak, D. Callahan-Miller, D. D. M. Ho, and G. B. Zimmerman, *Nucl. Fusion* **38**, 509 (1998).
 - [6] D. A. Callahan, *Appl. Phys. Lett.* **67**, L3254 (1995).
 - [7] J. Sasaki *et al.*, *Jpn. J. Appl. Phys.* **40**, L968 (2001).
 - [8] D. R. Welch, D. V. Rose, B. V. Oliver, T. C. Genoni, and R. E. Clark, *Phys. Plasmas* **9**, 2344 (2002).

- [9] T. Someya, S. Kawata, T. Nakamura, A. I. Ogoyki, K. Shimizu, and J. Sasaki, *Fusion Sci. Tech.* **43**, 282 (2003).
- [10] National Research Council of the National Academies, U.S.A., R. C. Davidson *et al.*, *High Energy Density Physics* (The National Academies Press, Washington, DC, 2003), p. 131.
- [11] W. M. Sharp *et al.*, *Fusion Sci. Tech.* **43**, 393 (2003).
- [12] M. Murakami, *Appl. Phys. Lett.* **27**, 1587 (1995).
- [13] M. Murakami, K. Nishihara, and H. Azechi, *J. Appl. Phys.* **74**, 802 (1993).
- [14] S. Skupsky and K. Lee, *J. Appl. Phys.* **54**, 3662 (1983).
- [15] S. Kawata and K. Niu, *J. Phys. Soc. Jpn.* **53**, 3416 (1984).
- [16] M. H. Emery, J. H. Orens, J. H. Gardner, and J. P. Boris, *Phys. Rev. Lett.* **25**, 253 (1982).
- [17] G. A. Magelssen and W. P. Gula, *Phys. Fluids* **25**, 898 (1982).
- [18] R. W. Petzoldt, *Fusion Technol.* **34**, 831 (1998).
- [19] H. H. Andersen and J. F. Ziegler, *The Stopping and Ranges of Ion in Matter* (Pergamon Press, New York, 1977), Vol. 3.
- [20] F. C. Young, D. Mosher, S. J. Stephanakis, S. A. Goldstein, and T. A. Mehlhorn, *Phys. Rev. Lett.* **49**, 549 (1982).
- [21] K. A. Long and N. A. Tahir, *Phys. Rev. A* **35**, 2631 (1987).
- [22] T. A. Mehlhorn, Sandia National Laboratories Report No. SAND80-0038, 1980.
- [23] J. A. Swegle, Sandia National Laboratories Report No. SAND82-0072, 1982.
- [24] T. A. Mehlhorn, J. M. Peek, E. J. Mcguire, J. N. Olsen, and F. C. Young, Sandia National Laboratories Report No. SAND83-1519, 1983.
- [25] T. Peter and J. Meyer-ter-Vehn, *Phys. Rev. A* **43**, 1998 (1991).
- [26] T. Peter and J. Meyer-ter-Vehn, *Phys. Rev. A* **43**, 2015 (1991).
- [27] M. Murakami and J. M. Vehn, *Nucl. Fusion* **31**, 1333 (1991).
- [28] P. Wang, T. M. Mehlhorn and J. J. MacFarlane, *Phys. Plasmas* **5**, 2977 (1998).
- [29] K. A. Long and N. A. Tahir, *Phys. Lett. A* **91**, 451 (1982).
- [30] J. Lindhard and M. Schaff, *Phys. Rev.* **124**, 128 (1961).
- [31] R. A. Sacks, R. C. Arnold, and G. R. Magelssen, *Nucl. Fusion* **22**, 1421 (1982).